



UvA-DARE (Digital Academic Repository)

Fluorescent molecular rotors

From working principles to visualization of mechanical contacts

Suhina, T.

Publication date

2017

Document Version

Other version

License

Other

[Link to publication](#)

Citation for published version (APA):

Suhina, T. (2017). *Fluorescent molecular rotors: From working principles to visualization of mechanical contacts*. [Thesis, fully internal, Universiteit van Amsterdam].

General rights

It is not permitted to download or to forward/distribute the text or part of it without the consent of the author(s) and/or copyright holder(s), other than for strictly personal, individual use, unless the work is under an open content license (like Creative Commons).

Disclaimer/Complaints regulations

If you believe that digital publication of certain material infringes any of your rights or (privacy) interests, please let the Library know, stating your reasons. In case of a legitimate complaint, the Library will make the material inaccessible and/or remove it from the website. Please Ask the Library: <https://uba.uva.nl/en/contact>, or a letter to: Library of the University of Amsterdam, Secretariat, Singel 425, 1012 WP Amsterdam, The Netherlands. You will be contacted as soon as possible.

Excited-state Decay Pathways of DCDHF Molecular Rotors: Twisted Intermediate or Conical Intersection?*

Abstract

The fluorescence intensity of molecular rotors containing the dicyanodihydrofuran (DCDHF) motif increases strongly with solvent viscosity. Single-bond and double-bond rotations have been proposed as pathways of nonradiative decay for this and related molecular rotors. In this work, we use steady-state and time-resolved fluorescence measurements and combine them with visible-pump/mid-IR probe transient measurements. Combination of these powerful techniques enables us to learn more about the excited state dynamics of **1** in a range of solvents. To further deepen our fundamental understanding of the relevant processes, we supplement our experimental findings with TD-DFT calculations. We show here that both single and double bond rotations are involved in the case of DCDHF rotors: fluorescence is quenched by rotation around the dicyanomethylene double bond in non-polar solvents, but in a sufficiently polar environment rotation about a formally single bond leads to a dark internal charge-transfer state.

*This chapter is adapted from:

Suhina, T; Amirjalayer, S.; Mennucci, B.; Woutersen, S.; Hilbers, M.; Bonn, D.; Brouwer, A. M. *The Journal of Physical Chemistry Letters* **2016**, 7, 4285-4290.

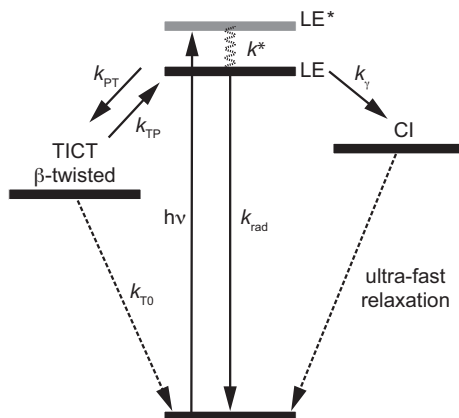


Figure 4.1: Proposed model for fluorescence deactivation of **1**.

The two proposed fluorescence deactivation pathways of **1** and **2** are presented in Fig. 4.1. After initial photo-excitation from the ground state (GS) and fast relaxation processes (with rate constant k^*), the molecule reaches the near-planar LE state. From there it can radiatively relax to the ground state (k_{rad}), or perform twisting motion around either the γ (k_{γ})²¹ or β (k_{PT}) bond (see Scheme 4.1). Both twists result in fluorescence deactivation. Twisting around γ leads to a conical intersection (CI) with the ground state potential energy surface (PES) and instantaneous nonradiative relaxation. Twisting around the β bond yields a highly polar twisted intramolecular charge-transfer (TICT)²⁵ state. This state has a finite lifetime, and it can either act as a sink (it converts to the GS directly with rate constant k_{T0}) or as a reservoir state (TICT back-converts to the LE state and to the GS with rate constants k_{TP} and k_{T0} , respectively). In the latter case delayed fluorescence occurs and causes biexponential fluorescence decays. These twists occur easily in liquid solvents, but become hindered as solvent viscosity is increased. In this way, the degree of confinement is reflected by a fluorescence response. Below we show that the deactivation pathway of **1** strongly depends on solvent polarity: deactivation proceeds through CI (through γ twist in Scheme 4.1) in non-polar solvents, whereas polar solvents facilitate formation of the TICT species and subsequent deactivation (through β twist, Scheme 4.1).

4.2 Experimental

Most of experimental details regarding the setups used can be found in Chapter 2. Experimental details that are specific to this chapter are described below.

All solvents used were of HPLC grade or spectroscopic grade. DMSO and MeCN were dried over 4 Å molecular sieves and passed through activated Al_2O_3 before use. Toluene was distilled from CaH_2 prior to use and stored over molecular sieves under N_2 atmosphere. EtOAc was stirred with K_2CO_3 for 30 minutes, passed over activated Al_2O_3 , distilled and stored over 4 Å molecular sieves under N_2 atmosphere. Compound **1** was prepared according to the previously reported

procedure.²⁶

Transient data analysis

The obtained transient matrices were analyzed with Glotaran,^{27,28} Matlab equipped with UltraFast Toolbox,²⁹ and with the help of SVD techniques discussed in Chapter 2.³⁰ In all cases, SVD was used in order to reduce artifacts and noise. The number of components used in filtering was determined by looking at their left and right singular vectors (weighted by their respective singular values). If no significant structure was observed, SVD components were not used in reconstruction of the data set. The reconstructed dataset was subsequently compared to the original dataset in order to check whether any significant information was lost during the filtering process. In all cases, a Gaussian-shaped IRF (fwhm \sim 200 fs) was obtained and used for iterative reconvolution of the measured time traces.

Calculations

All calculations were performed on a model molecule **1a**, in which hexyl chains were replaced with methyl groups in order to reduce calculation costs, (Scheme 4.1) with CAM-B3LYP/6-31+G(d) level of theory.³¹ Solvent effects were included through the Integral Equation Formalism³² version of the Polarizable Continuum Model (PCM).³³ Relaxed excited state potential energy surfaces were obtained assuming a complete relaxation of the solvent polarization. To account for a proper response of the solvent, a state-specific correction has been introduced for each point of the PESs through the cLR formulation.³⁴ All calculations have been performed with a locally modified version of Gaussian '09 software.³⁵

4.3 Results and discussion

4.3.1 Fluorescence quantum yields and solvent polarity response

The steady-state absorption and fluorescence spectra of **1** (see Figure 4.2 a)) show significant changes both in the shape and peak positions as solvents are changed from non-polar hexane to the highly polar DMSO, indicating charge-transfer character of the excited state. We have experimentally estimated the difference in the ground and excited state dipole moments by employing a polarizable point dipole dielectric continuum model, which takes into account the polarizability of the solute (see Chapter 2.1.5).^{22,23,36} From the Stokes shifts we estimate the difference in dipole moments of S_1 and S_0 to be $\Delta\mu = 5.8 \pm 0.9$ D. Due to efficient fluorescence deactivation, quantum yields in liquids are very low (see Table 4.1). In the very polar solvents DMSO and MeCN the quantum yields (Φ_f) are less than 1%. The quantum yield is somewhat higher in medium polarity EtOAc (2.9%) and peaks in the relatively non-polar toluene (5.0%). An order-of-magnitude drop in Φ_f (\sim 0.6%) is observed when going from toluene to the even less polar hexane (see

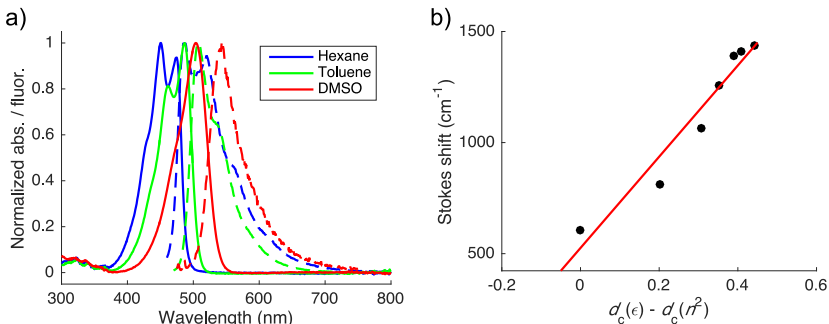


Figure 4.2: a) Absorption and emission spectra of **1** in selected solvents; b) Stokes shifts of **1** in hexane, chloroform, dichloromethane, benzonitrile, DMSO, acetone, and acetonitrile.

Table 4.1: Fluorescence properties of **1** at room temperature (24 °C).

solvent	η^a (cP)	ϵ_r^a	Φ_f^b (%)	$k_{\text{rad}}^d 10^8$ (s ⁻¹)	τ_{pred}^e (ps)	$M_{01/10}^f$ (D)	$\epsilon_{\text{max,abs}}^g$ (M ⁻¹ cm ⁻¹)	$\lambda_{\text{max,abs}}^h$ (nm)	$\lambda_{\text{max,em}}^h$ (nm)
hexane	0.30	1.9	~ 0.6	2.8	~ 20	7.33	59900	474*	486**
toluene	0.56	2.4	5.0	3.1	160	6.74	62200	487	509
EtOAc	0.42	6.0	2.9 ^c	2.8	46	7.85	68000	488	522
MeCN	0.37	36.6	~ 0.3	2.8	11	8.10	75800	495	532
DMSO	1.99	46.8	~ 0.5	3.0	17	7.24	76000	504	541

^a Values for relative permittivity (ϵ_r) and viscosity at room temperature (η) obtained from ref. 37; ^b Fluorescence quantum yields (%); fluorescein in 0.1 M NaOH ($\Phi_f=0.89$ ³⁸) was used as a reference; ^c Φ_f obtained from ref 16. ^d Radiative rates from the Strickler-Berg expression³⁹; ^e Fluorescence lifetimes calculated as Φ_f/k_{rad} ; ^f Absorption and emission transition dipole moments obtained from Eqs. 2.4 and 2.5; ^g Molar absorption coefficient at absorption maximum; ^h Location of absorption and emission maxima; * Lowest energy peak; ** Highest energy peak.

Figure 4.3). This trend can be explained by the presence of two different barriers with different polarity dependencies that lead to fluorescence deactivation.

4.3.2 Fluorescence decay times

The fluorescence decays show trends similar to the quantum yields observed in steady-state measurements. In hexane and isooctane, the decays are too fast to be measured with our TCSPC equipment. In toluene, global fit of the 12 fluorescence decay curves resulted in a single fluorescence decay time constant of 120 ps (see Fig. 4.4). Our calculations (see below) indicate that the increase in polarity (which occurs in the case of toluene *vs* hexane) results in an increase of the energy barrier that separates the LE state from the CI, and explains longer fluorescence lifetime measured in toluene. In EtOAc, the decay is biexponential with time constants of $\tau_1 = 30$ and $\tau_2 = 228$ ps at room temperature (Fig. 4.4 b)) which were obtained by a global fit of 6 fluorescence decays. Reconstructed decay-associated fluorescence spectra show two components with identical spectral profiles (Fig. 4.5 a)), indicating that fluorescence emission occurs from a single state. In DMSO, fitting decays with a single time constant resulted in χ^2 values

Figure 4.3: Fluorescence quantum yield of **1** as a function of solvent polarity function $d_c(\epsilon)$.

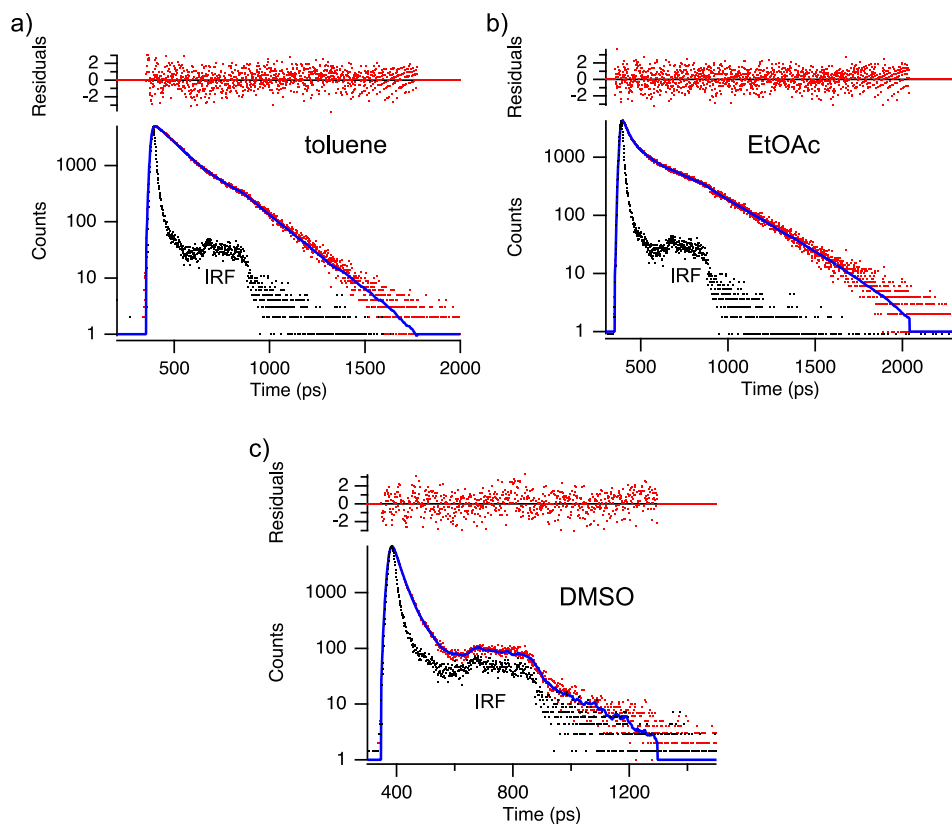
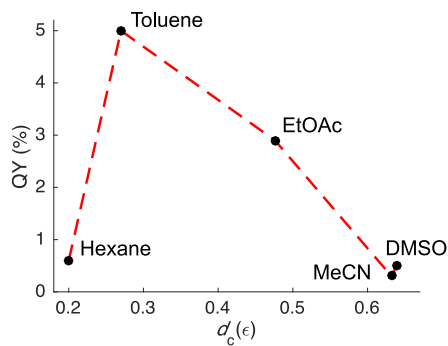


Figure 4.4: Fluorescence decays (black) and fits (blue) of **1** measured in: a) toluene; b) EtOAc; and c) DMSO.

> 1.4 and significant structure in the residuals. For this reason, we used a second exponent to fit 8 measured curves (see Fig. 4.4 c)). This fit resulted in decay time constants of 10 and 30 ps. Normalized decay associated fluorescence spectra associated with these time constants are shown in Fig. 4.5 b). Although the fit quality is not completely satisfactory, adding more exponential components does not significantly improve the overall quality of the fit. The reconstructed spectrum associated with the short component (10 ps) is blue shifted relative to the one associated with the longer (30 ps) component, and indicates the presence of solvation dynamics. Dynamic Stokes shifts are expected due to a significant charge-transfer character of **1** and typically occur on time scales shorter than 10 ps.⁴⁰ Since the fluorescence lifetime of **1** is very short (see Fig. 4.4 c)), the presence of IRF artifacts and IRF drift during the (due to low Φ_f in DMSO, relatively long) photon collection process have a significant influence on the values of the recovered time constants (see ref. 41 for additional details), and in our case make the short time constant appear longer than it actually is (see Chapter 5 for additional insight provided by vis pump-probe experiments).

The trend obtained from calculations presented below and the obtained decay associated fluorescence spectra suggest that EtOAc is just polar enough to prevent crossing at the energy barrier leading to the CI (the γ twist becomes hindered) and to simultaneously lower the energy barrier that separates the LE state from the β -twisted (TICT) state. It is, however, not polar enough to stabilize the TICT state to such an extent that it cannot convert back to the fluorescent planar LE state. As a result of this interconversion we observe delayed fluorescence. The kinetic model (see Scheme 4.1) can be expressed by the following equations:

$$\frac{\partial[P]}{\partial t} = k_{TP}[T] - k_{PT}[P] - k_{rad}[P], \quad (4.1)$$

$$\frac{\partial[T]}{\partial t} = k_{PT}[P] - k_{TP}[T] - k_{T0}[T], \quad (4.2)$$

$$[GS] = 1 - [P] - [T], \quad (4.3)$$

(with P , T and GS the LE planar, β -twisted TICT, and ground state, respectively), which can be solved analytically, so that k_{PT} , k_{TP} and k_{T0} can be obtained from our data. k_{PT} and k_{TP} represent the rate constants for conversion of planar to twisted, and twisted to planar species. In this case, initial conditions for $[P]$, $[T]$ and $[GS]$ are: $[P](t = 0) = 1$ and $[T](t = 0) = [GS] = 0$. Solving this system of equations leads to analytical expressions for $[P]$, $[T]$ and $[GS]$. The time evolutions of concentration $[P]$ can be expressed in terms of two exponential functions that contain fluorescence decay rates (k_1 and k_2) with associated amplitudes (A_1 and A_2 , where $A_2 = 1 - A_1$ due to the boundary condition $[P](t = 0) = 1$). See equations 4.4 and 4.5 for the final expressions that were obtained this way. In these expressions X and Y are substitution terms defined as $X = k_{rad} + k_{PT}$ and $Y = k_{TP} + k_{T0}$. Similar expressions have been derived in the literature to study kinetics of e.g. dimethyl amino benzonitrile.⁴² Having this in mind, fitting fluorescence decays (which yields A_1 , A_2 , k_1 and k_2) allows us to calculate values

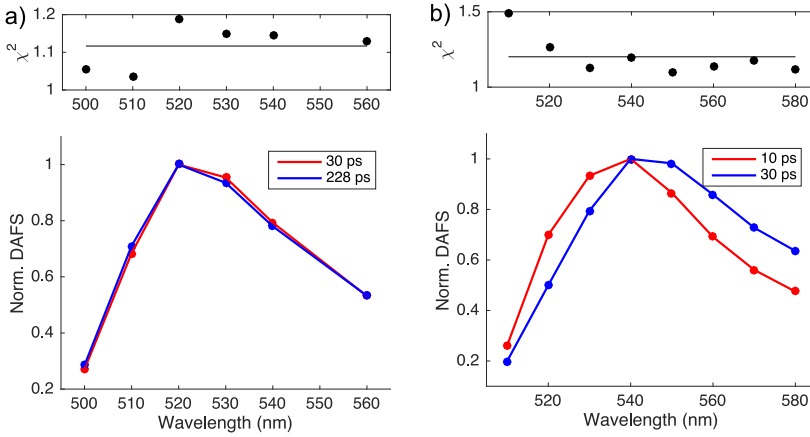


Figure 4.5: Decay associated fluorescence spectra of **1** in: a) EtOAc and b) DMSO.

for k_{PT} , k_{TP} and k_{T0} . Here we assume that $k_{\text{rad}} = 3.8 \times 10^{-8} \text{ s}^{-1}$, based on the average lifetime obtained by measuring the fluorescence decays of **1** in PVOAc matrix. The k_{PT} and k_{TP} values (2.5×10^{10} and $4.5 \times 10^9 \text{ s}^{-1}$ at room temperature, respectively) thus obtained allow estimation of the energy of the TICT state to be $\sim 0.9 \text{ kcal/mol}$ lower than the energy of the planar LE state at room temperature for **1** in EtOAc.

$$k_{1/2} = \frac{X + Y \pm (\sqrt{X^2 - 2XY + Y^2 + 4k_{PT}k_{TP}})}{2} \quad (4.4)$$

$$A_1 = \frac{X - k_2}{k_1 - k_2}; A_2 = 1 - A_1 \quad (4.5)$$

4.3.3 Temperature experiments

Fluorescence emission spectra of **1** in EtOAc measured at increasing temperatures show an unusual increase of intensity (Figure 4.6). To further investigate this, we have measured fluorescence decays for **1** in EtOAc at different temperatures and obtained relevant rates according to Eqs. 4.4 and 4.5 (see Table 4.2 and Fig. 4.7 a)).

The driving force (ΔG , Eq. 4.6) for the reaction $P \rightarrow T$ decreases with temperature (Fig. 4.7 b)), which means that the TICT (T) state becomes energetically less favorable at higher temperatures. The reason for this is that the dielectric constant of EtOAc decreases upon temperature increase (from ~ 6.4 at $5.5 \text{ }^\circ\text{C}$ to ~ 5.4 at $50 \text{ }^\circ\text{C}$ ³⁷). Since the TICT (T) state is more polar than the LE (P) state, the decrease in dielectric constant results in destabilization of the TICT state relative to the LE state upon heating. Fitting the data in Table 4.2 with Eq. 4.7 (van 't Hoff equation) produces values of $\Delta H^0 = -3.9 \pm 0.15 \text{ kcal/mol}$ and ΔS

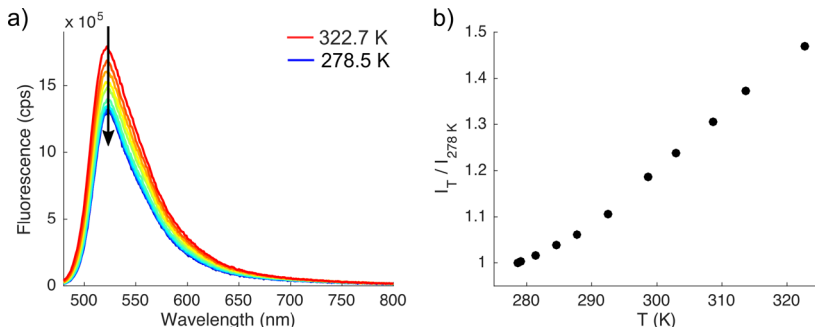


Figure 4.6: Fluorescence response of **1** upon heating in EtOAc: a) Fluorescence spectra; b) Normalized total intensity.

$= -9.8 \pm 0.5 \text{ cal mol}^{-1}\text{K}^{-1}$ (Fig. 4.6 c)). The negative value of ΔS is due to increased solvation of the TICT state which causes the decrease in overall entropy.

$$\Delta G = -RT \ln \left(\frac{k_{\text{PT}}}{k_{\text{TP}}} \right) \quad (4.6)$$

$$\ln \left(\frac{k_{\text{PT}}}{k_{\text{TP}}} \right) = -\frac{\Delta H^0}{RT} + \frac{\Delta S}{R} \quad (4.7)$$

The twisting rates k_{PT} and k_{TP} increase with temperature, while k_{T0} somewhat counterintuitively decreases. This causes the shorter time constant (τ_1) to decrease (from 37 ps at 5.5°C to 25 ps at 54.5°C) and the longer one (τ_2) to increase (from 168 ps at 5.5°C to 282 ps at 54.5°C) with temperature. Two factors contribute to the increase of Φ_f with increasing temperature: 1) nonradiative relaxation of **1** in EtOAc occurs through the TICT state; the decrease in k_{T0} results in less efficient nonradiative decay; 2) the simultaneous increase of $k_{\text{TP}}/k_{\text{PT}}$ produces an increase in population of the fluorescent planar state [P]. The change in k_{T0} probably originates from the fact that increasing the temperature causes the relative permittivity of EtOAc to decrease, which in turn destabilizes the TICT state and separates it further from the ground state potential energy surface (PES) rendering nonradiative decay less rapid.⁴³ At the same time, the energy of the TICT state comes closer to the energy of the LE state, increasing k_{TP} . The increase in Φ_f and longer τ_2 with temperature (Figs. 4.6 b) and 4.7 a)) show that the escape through the alternative channel (γ twist) does not occur under these conditions. Further evidence for this is provided in Ch. 5.

Heating **1** in non-polar solvents causes fluorescence to decrease. This is because nonradiative relaxation occurs through γ twist (see Fig. 4.1), which leads to a conical intersection between the ground and excited state potential energy surfaces. In order to assess the activation barrier leading to the conical intersection (γ twist), we measured fluorescence intensities as a function of temperature in non-polar solvents toluene and hexane (in which we found no indication of TICT formation). In these solvents (over a reasonable range of temperatures) dielectric properties

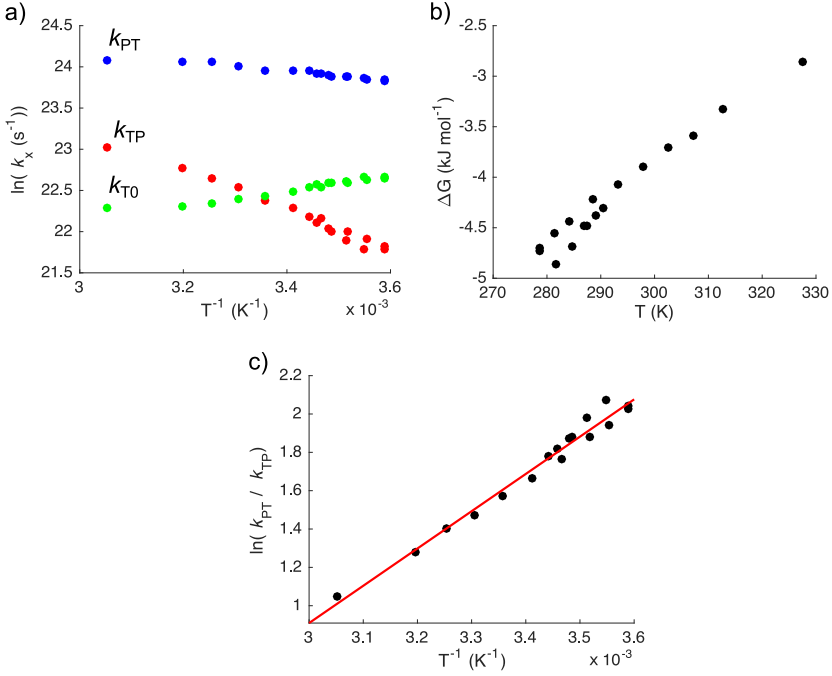


Figure 4.7: a) Obtained reaction rates as a function of temperature; b) Gibbs free energy difference between the LE and TICT state as a function of temperature; c) van 't Hoff plot with slope of $1945 \pm 75 \text{ K}^{-1}$ and intercept of -4.92 ± 0.55 .

are not expected to change considerably, allowing us to estimate the γ twist energy barrier with relatively small uncertainties and compare their values with results obtained from TD-DFT calculations (see below). The fluorescence deactivation rate constant k_γ can be expressed in terms of the fluorescence intensity, which is directly proportional to Φ_f . The fluorescence quantum yield can be expressed by Eq. 4.8, which can be rearranged to yield Eq. 4.9. If we assume that k_{rad} remains constant over the measured temperature range, and $1/\Phi_f \gg 1$ then fluorescence intensity will be inversely proportional to the twisting rate ($k_\gamma = k_{nr}$).

$$\Phi_f = \frac{k_{rad}}{k_{rad} + k_{nr}} \quad (4.8)$$

$$k_\gamma = \frac{k_{rad}}{\Phi_f} - k_{rad} = k_{rad} \left(\frac{1}{\Phi_f} - 1 \right) \quad (4.9)$$

By taking the Förster-Hoffmann equation⁴⁴ into account (see Eq. 4.10), the effect of viscosity change on fluorescence can be accounted for in an Arrhenius expression and Eq 4.11 is obtained.

$$\Phi_f = \text{constant} \times \eta^\alpha \quad (4.10)$$

$$\ln(k_\gamma) = \text{constant}_1 - \frac{E_a}{RT} - \text{constant}_2 - \alpha \times \ln(\eta(T)) \quad (4.11)$$

Table 4.2: Rate constants obtained from Eqs. 4.4 and 4.5 for **1** in EtOAc measured at different temperatures.

T (K)	k_{PT} (10^9 s $^{-1}$)	k_{TP} (10^9 s $^{-1}$)	k_{T0} (10^9 s $^{-1}$)	ϵ_r ³⁷
278.65	22.89	3.02	6.92	6.41
281.45	22.88	3.27	6.88	6.34
281.75	22.94	2.89	6.70	6.34
284.25	23.46	3.59	6.92	6.28
284.65	23.59	3.25	6.47	6.27
286.85	23.56	3.60	6.64	6.23
287.35	24.09	3.69	6.44	6.22
288.55	24.39	4.19	6.47	6.19
289.15	24.54	3.97	6.18	6.18
290.45	25.34	4.27	6.34	6.15
293.15	25.31	4.78	6.17	6.09
297.75	25.35	5.26	5.84	6.00
302.45	26.74	6.12	5.55	5.90
307.25	28.02	6.87	5.30	5.80
312.75	28.03	7.82	5.08	5.69
327.65	28.76	10.05	4.83	5.41

Since the viscosities of hexane and toluene show Arrhenius-type behavior and thus follow equation 4.12,⁴⁵ we finally arrive at Eq.4.13.

$$\ln(\eta) = \frac{B}{RT} + \text{constant} \quad (4.12)$$

$$\ln(k_\gamma) = \text{constant} - \frac{E_a}{RT} - \alpha \left(\frac{B}{RT} \right) \quad (4.13)$$

We assume the value of Förster-Hoffmann (FH) pre-exponential factor $\alpha = 2/3$ based on our previous work.¹⁶ We note, however, that this value was obtained by measuring fluorescence response to viscosity in polar solvent (MeCN) for **2**, and FH pre-exponential factors might differ in non-polar hexane and toluene. Although this might introduce some error, this error is significantly smaller than ignoring the viscosity effect completely. Viscosity barriers (B) for hexane and toluene are obtained by fitting the experimental viscosity data³⁷ to Eq. 4.12. These parameters are used in Eq. 4.13, where $\ln(k_\gamma)$ is replaced with $\ln(1/I_{\text{tot}})$ (because of Eq 4.9 and the fact that $k_{nr} \gg k_{\text{rad}}$).

Linear fits produce activation energy barriers for γ isomerization of 3.59 ± 0.07 and 3.62 ± 0.19 kcal/mol for hexane and toluene, respectively. If the value of α is taken to be 1, the activation barrier values drop to 3.04 ± 0.07 and 2.9 ± 0.19 . One needs to keep in mind that these barriers are overestimated, since the barrier response to the change in dielectric constant can't be determined with the currently available data.

Figure 4.8: Natural logarithm of total intensity *vs* inverse temperature for **1** in hexane and toluene. Lines represent fits obtained through Eq. 4.13.

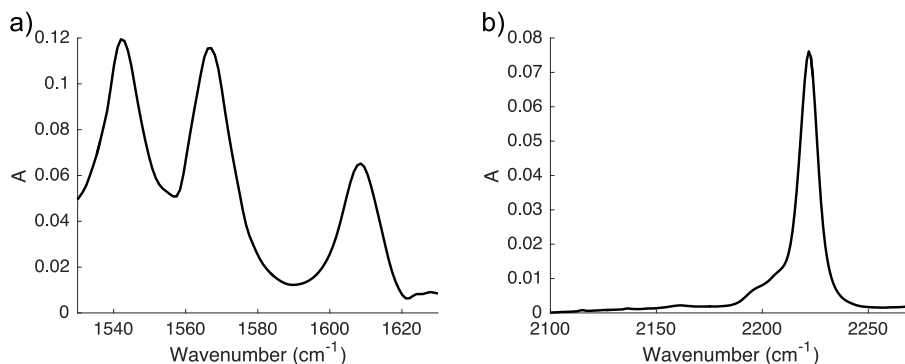
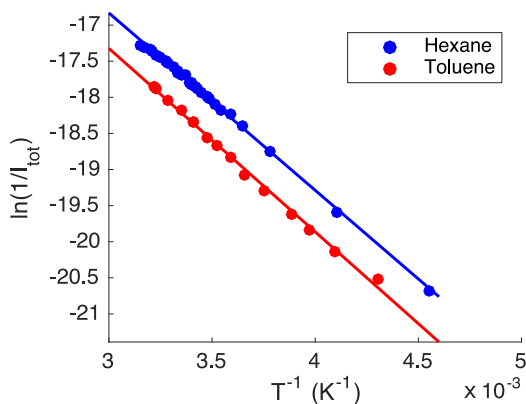


Figure 4.9: FTIR spectra of **1** in DMSO: a) C=C region; b) CN region.

4.3.4 Vis-pump/mid-IR probe experiments

In DMSO, the TICT state (β -twisted structure in Fig. 4.3) is readily formed and does not revert back to the fluorescent LE planar state. Formation of the β -twisted transient species in polar DMSO can be observed in vis-pump/mid-IR probe measurements (time resolution ~ 200 fs).

IR spectra of solutions of **1** in DMSO in the C=C and CN regions are shown in Fig. 4.9. Transient IR spectral traces in the same regions are shown in Figure 4.10 a). Representative time traces are shown in Figure 4.10 b). In the C=C region, ground-state bleach (GSB) bands are centered at 1568 and 1608 cm^{-1} . Another GSB band is centered at 1542 cm^{-1} but its strong overlap with excited-state absorption (ESA) bands originating from the planar LE state makes it visible only at later probe delays. An excited state band rises at 1582 cm^{-1} , and we attribute it to the formation of the β -twisted TICT state. Its rise correlates with the decay of LE ESA bands centered at 1535 and 1552 cm^{-1} (Figures 4.10 a) and b)), indicating sequential formation kinetics. A spectral signature of this species can also be observed in the CN stretch region (see Figures 4.10 a) and 4.10 c)).

The TICT state manifests itself here as a rise in the ESA, but very pronounced overlap between the CN bands (symmetric and asymmetric stretches) of the LE and TICT states complicates the separation of the bands associated with the two species. From a global fit of the transient data with a target sequential model⁴⁶ (see Eq. 4.14) we reconstruct species-associated spectra (shown in Figure 4.10 c)), with rate constants of $k_{\text{PT}}=(3.68 \pm 0.06)\times 10^{10} \text{ s}^{-1}$ and $k_{\text{T0}}=(9.85 \pm 0.03)\times 10^{10} \text{ s}^{-1}$ (k^* was too fast to be resolved).



Vis-pump/mid-IR probe measurements for **1** in toluene do not indicate the presence of transient species. Global analysis with the sequential model yields two rate constants of $(1.31 \pm 0.07)\times 10^{12} \text{ s}^{-1}$ and $(8.32 \pm 0.02)\times 10^9 \text{ s}^{-1}$ (Fig. 4.11). We attribute the shorter one to vibrational cooling and the longer one to the decay of the fluorescent LE state. These rates show excellent agreement with the fluorescence measurements and indicate that fluorescence deactivation of **1** indeed proceeds through a conical intersection and does not involve transient intermediates.

4.3.5 Calculations

In order to gain a more fundamental understanding of the photophysical processes of **1**, we performed calculations at the CAM-B3LYP/6-31+G(d) level of theory. Although this functional is known to overestimate vertical excitation energies, it provides a good qualitative description of systems with a significant charge-transfer character.⁴⁷ To further validate the results, potential energy surface (PES) scans were repeated with $\omega\text{B97DX}/6\text{-}31\text{+G(d)}$ ⁴⁸ (not shown), but the obtained trends remained the same.

Figure 4.12 shows the optimized ground state geometry that was obtained for **1a** in DMSO. Geometries obtained in vacuum and toluene are similar, with small variations in benzene-furan (β) and furan-C-CN (γ) dihedral values. These small structural variations are accompanied by the increase in ground state dipole moments from vacuum (16.6 D), through toluene (20.0 D) to DMSO (24.1 D). The dipole moments further increase in the excited state (to 18.0 D, 23.7 D and 29.5 D, respectively), which is indicated by a pronounced shift in electron density to the acceptor part in the LUMO (Fig. 4.12 b) and c)). Calculated $\Delta\mu$ are somewhat smaller (2.0, 3.7 and 5.4 D for vacuum, toluene and DMSO, respectively) than the experimentally obtained value of ~ 5.8 D.

Relaxed scans of the excited state PES obtained by means of TD-DFT (CAM-B3LYP/6-31+G(d)) and PCM solvation show excellent agreement with our experimental results. TD-DFT calculations find three minima (see Fig. 4.13 and Fig. 4.14 a)-c)) on the S_1 PES. One minimum belongs to the fluorescent LE planar state (Fig. 4.14 a)) which is reached upon photo-excitation and subsequent geometry relaxation. The geometry of the locally excited (LE) state does not differ significantly from the ground state optimized geometry. There are, however, small

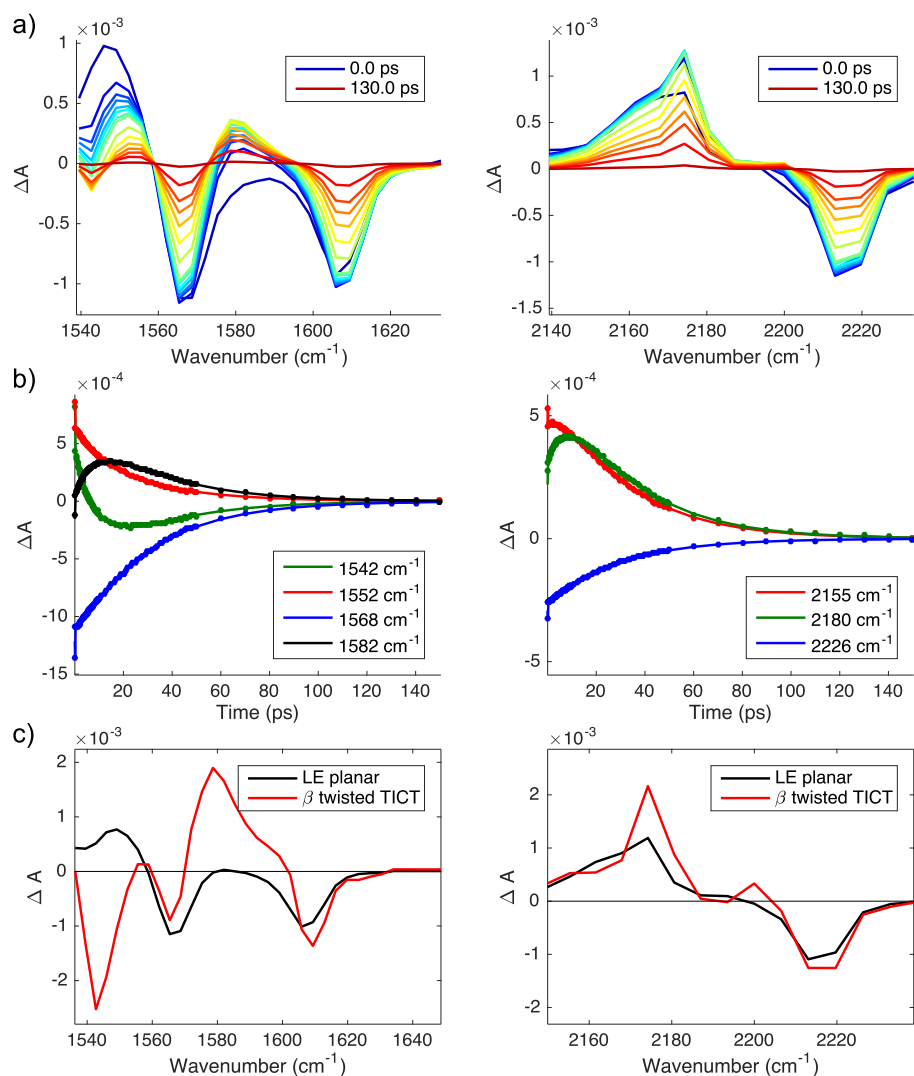


Figure 4.10: Visible-pump/mid-IR probe measurements on **1** in DMSO: a) Selected difference spectra at different delay times in C=C (left) and CN (right) regions; b) Representative time traces measured in C=C (left) and CN (right) stretch regions, respectively; c) Species associated spectra reconstructed from the global fit of the sequential model.

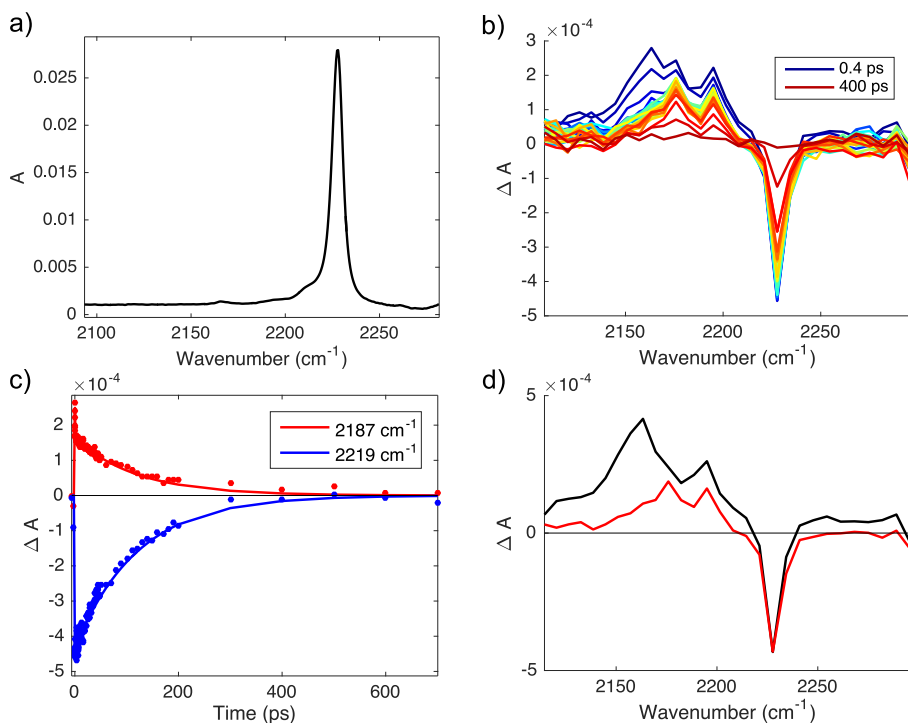


Figure 4.11: FTIR and visible-pump/mid-IR probe measurements on **1** in toluene: a) FTIR spectra of **1**; b) Selected wavelength traces; c) Representative time traces; d) Species associated spectra reconstructed from the global fit with the sequential model.

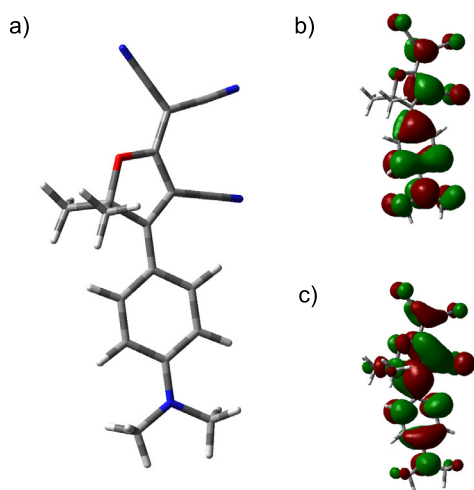


Figure 4.12: a) Ground state optimized geometry of **1a** in DMSO; b) Highest occupied molecular orbital; c) Lowest unoccupied molecular orbital.

differences from one solvent to another. In vacuum, the phenyl-furan dihedral angle (β) changes from 16.5 in the GS to 9.4 degrees in S_1 . At the same time, the furan-C-CN dihedral (γ) changes from -0.6 to -5.7. In DMSO, the β dihedral increases from 9.5 to 18.4 degrees, while γ changes from -0.9 to -3.1 degrees going from S_0 to S_1 .

The second PES minimum can be accessed through twisting of the β bond (Fig. 4.14 b)). This twist is accompanied by a large increase in the dipole moment relative to the LE state geometry in toluene and DMSO (23.7 \rightarrow 33.7 D and 29.5 \rightarrow 38.8 D, respectively). This results in polar solvents lowering the energy barrier that leads to the twisted state (\sim 3.7 kcal/mol in vacuum, \sim 1.3 kcal/mol in toluene, \sim 0.1 kcal/mol in DMSO). As the β -twisted TICT state becomes easier to reach, the back conversion from the TICT to the planar fluorescent state becomes increasingly more difficult as the environment polarity increases. The energy difference between the GS and ES β -twisted geometries decreases as the polarity increases (from 52 kcal mol $^{-1}$ in toluene to 29 kcal mol $^{-1}$ in DMSO), but the surfaces remain well separated and the oscillator strength decreases gradually with increasing β dihedral values. We have found no evidence for a CI near these coordinates. Instead, nonradiative relaxation from this state is expected (and experimentally observed) to become more efficient as the solvent polarity increases due to the decreasing distance of the two surfaces (energy-gap law).⁴³ The trends obtained from the TD-DFT calculations are in excellent agreement with our experimental observations which show that the reversible β twist occurs in solvents of medium polarity (EtOAc) and becomes irreversible in highly polar solvents (DMSO, MeCN) due to stabilization of the TICT state.

The third minimum is reached by twisting about the γ bond (see Fig. 4.14 c)). This twist causes a remarkable decrease in the calculated ES dipole moments (23.7 \rightarrow 12.4 D and 29.5 \rightarrow 13.3 D, in toluene and DMSO, respectively), and is characterized by a drop in oscillator strength at $\gamma \sim 40 - 60^\circ$. Due to the dipole moment decrease, polar solvents are expected to hinder this twist. Such a trend was observed previously by Massin *et al.*, who used a deactivation through a dicyanomethylene twist of a functionally similar probe to monitor the polarity of the surrounding medium.⁴⁹ The calculated energy barrier for this twist is \sim 3.1 kcal/mol for **1a** in toluene and 5.8 kcal/mol in DMSO. We have experimentally estimated this barrier to be \sim 3.6 kcal mol $^{-1}$ in hexane ($\epsilon_r=1.89$) and toluene ($\epsilon_r=2.38$). This value is reasonably close to the calculated value of 3.1 kcal mol $^{-1}$ obtained for toluene.

These findings indicate two important things: 1) twisting about β does not lead to conical intersection, but to the TICT state as a local minimum. This state is more stabilized by polar solvents, and since the dipole moment gradually increases as twist proceeds, the activation barrier which needs to be overcome to reach this state becomes lower with increasing solvent polarity. This twisting is accompanied by a gradual decrease in oscillator strength, indicating that the TICT state is a dark state. Our experiments show excellent agreement with this since we observed emission only from the LE state, but we could observe dark transient species in case of polar solvents. 2) Twisting about the γ bond results in an abrupt drop in

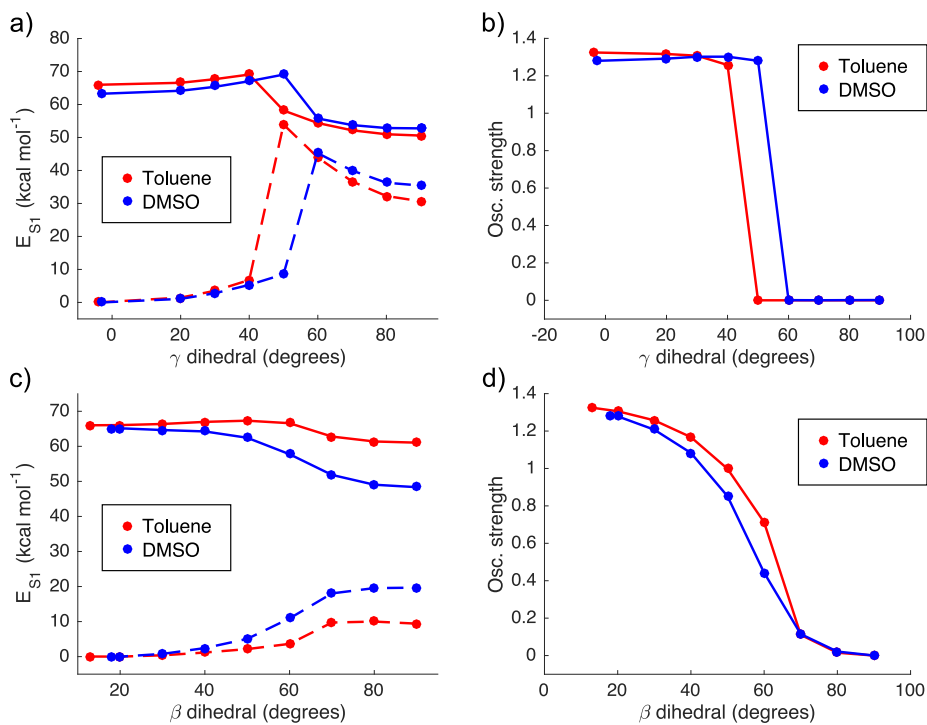
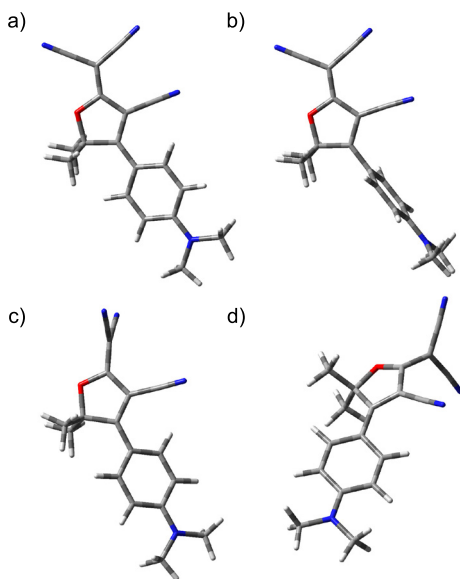


Figure 4.13: Partial potential energy surface scans of **1a** with polarizable continuum model solvation. The S_1 geometry was optimized for fixed values of the dihedral. S_0 energies were calculated at these geometries. a) Relaxed γ -constrained scan; b) Oscillator strength associated with the geometries produces by fixing γ dihedral angle; c) Relaxed β -constrained scan; d) Oscillator strength associated with the geometries produces by fixing β dihedral angle.

Figure 4.14: Optimized excited state geometries of **1a** in DMSO: a) Locally excited state optimized structure; b) β twisted (TICT) optimized structure; c) γ -twisted optimized structure d) Partially relaxed ($\gamma = 60^\circ$) structure near conical intersection.



oscillator strength ($\gamma \sim 40 - 50^\circ$ in toluene, $\gamma \sim 50 - 60^\circ$ in DMSO) accompanied by an increase of molecular dipole moment (which explains the energy barrier difference in non-polar and polar solvents). GS and ES PESs at the same time come very close together, which is accompanied by pyramidization of the furan ring carbon connecting dicyanomethylene group with the rest of the molecule (see Figure 4.14 d)). All this suggests the presence of a conical intersection between GS and ES at those coordinates which is expected to result in instantaneous GS repopulation. We stress that these results can be affected by the well-known limitations of TD-DFT in describing CI. However, a very good agreement is found with the experimental results which do not indicate formation of transient species in non-polar solvents, while a decrease in polarity (from toluene to hexane) results in more rapid excited-state decay.

4.4 Conclusion

To conclude, we have shown that **1** (and by analogy, **2**) can relax to the ground state via two distinct pathways. Both involve significant changes in geometry and account for the sensitivity of the fluorescence of these molecules to viscosity and free volume. The relaxation pathway depends strongly on the dielectric properties of the molecular environment: in non-polar solvents relaxation occurs by twisting about the exocyclic C=C (γ) bond, which results in momentary deactivation. Polar solvents hinder this twist, while at the same time opening up a new deactivation pathway that leads to the dark intermediate β twisted ICT state from which nonradiative relaxation occurs. The presence of two decay pathways leads

to a discontinuous dependence of the nonradiative decay rate at low viscosities on the polarity. Since the two pathways have different spatial requirements, the dependences of their rates on viscosity and free volume may be different. These factors need to be taken into account when molecular rotors similar to **1** are used as viscosity/free volume sensors.

References

1. Biancalana, M.; Koide, S. *Biochim. Biophys. Acta* **2010**, *1804*, 1405–1412.
2. Willets, K. A.; Ostroverkhova, O.; He, M.; Twieg, R. J.; Moerner, W. *J. Am. Chem. Soc.* **2003**, *125*, 1174–1175.
3. Lord, S. J.; Conley, N. R.; Lee, H.-l. D.; Samuel, R.; Liu, N.; Twieg, R. J.; Moerner, W. *J. Am. Chem. Soc.* **2008**, *130*, 9204–9205.
4. Lord, S. J.; Lu, Z.; Wang, H.; Willets, K. A.; Schuck, P. J.; Lee, H.-l. D.; Nishimura, S. Y.; Twieg, R. J.; Moerner, W. *J. Phys. Chem. A* **2007**, *111*, 8934–8941.
5. López-Duarte, I.; Vu, T. T.; Izquierdo, M. A.; Bull, J. A.; Kuimova, M. K. *Chem. Comm.* **2014**, *50*, 5282–5284.
6. Dent, M. R.; López-Duarte, I.; Dickson, C. J.; Geoghegan, N. D.; Cooper, J. M.; Gould, I. R.; Krams, R.; Bull, J. A.; Brooks, N. J.; Kuimova, M. K. *Phys. Chem. Chem. Phys.* **2015**, *17*, 18393–18402.
7. Rumble, C.; Rich, K.; He, G.; Maroncelli, M. *J. Phys. Chem. A* **2012**, *116*, 10786–10792.
8. Mustafic, A.; Huang, H.-M.; Theodorakis, E. A.; Haidekker, M. A. *J. Fluoresc.* **2010**, *20*, 1087–1098.
9. Mustafic, A.; Elbel, K. M.; Theodorakis, E. A.; Haidekker, M. *J. Fluoresc.* **2015**, *25*, 729–738.
10. Loutfy, R. O. *Macromolecules* **1981**, *14*, 270–275.
11. Royal, J. S.; Torkelson, J. M. *Macromolecules* **1990**, *23*, 3536–3538.
12. Royal, J. S.; Torkelson, J. M. *Macromolecules* **1992**, *25*, 1705–1710.
13. Dreger, Z.; Lang, J.; Drickamer, H. *Chem. Phys.* **1993**, *169*, 351–359.
14. Dreger, Z.; White, J.; Drickamer, H. *Chem. Phys. Lett* **1998**, *290*, 399–404.
15. Jee, A.-Y.; Bae, E.; Lee, M. *J. Phys. Chem. B* **2009**, *113*, 16508–16512.
16. Suhina, T.; Weber, B.; Carpentier, C. E.; Lorincz, K.; Schall, P.; Bonn, D.; Brouwer, A. M. *Angew. Chem. Int. Ed.* **2015**, *54*, 3688–3691.
17. Abdel-Mottaleb, M.; Loutfy, R. O.; Lapouyade, R. *Photochem. Photobiol. A* **1989**, *48*, 87–93.
18. Howell, S.; Dakanali, M.; Theodorakis, E. A.; Haidekker, M. A. *J. Fluoresc.* **2012**, *22*, 457–465.
19. Zhang, W.; Lan, Z.; Sun, Z.; Gaffney, K. J. *J. Phys. Chem. B* **2012**, *116*, 11527–11536.

20. Mqadmi, S.; Pollet, A. *Photochem. Photobiol. A* **1990**, *53*, 275–281.
21. Willets, K. A.; Callis, P. R.; Moerner, W. *J. Phys. Chem. B* **2004**, *108*, 10465–10473.
22. Jin, H.; Liang, M.; Arzhantsev, S.; Li, X.; Maroncelli, M. *J. Phys. Chem. B* **2010**, *114*, 7565–7578.
23. Dahl, K.; Biswas, R.; Ito, N.; Maroncelli, M. *J. Phys. Chem. B* **2005**, *109*, 1563–1585.
24. Haidekker, M.; Brady, T.; Lichlyter, D.; Theodorakis, E. *Bioorg. Chem.* **2005**, *33*, 415–425.
25. Grabowski, Z. R.; Rotkiewicz, K.; Rettig, W. *Chem. Rev.* **2003**, *103*, 3899–4032.
26. Gubler, U.; He, M.; Wright, D.; Roh, Y.; Twieg, R.; Moerner, W. *Adv. Mater.* **2002**, *14*, 313–317.
27. Mullen, K. M.; Van Stokkum, I. H. *J. Stat. Softw.* **2007**, *18*, 1–46.
28. Snellenburg, J.; Laptanok, S.; Seger, R.; Mullen, K.; Van Stokkum, I. *J. Stat. Softw.* **2012**, *49*.
29. van Wilderen, L. J.; Lincoln, C. N.; van Thor, J. J. *PLoS One* **2011**, *6*, 17373.
30. Henry, E. R. *Biophys. J.* **1997**, *72*, 652–673.
31. Yanai, T.; Tew, D. P.; Handy, N. C. *Chem. Phys. Lett.* **2004**, *393*, 51–57.
32. Cancès, E.; Mennucci, B.; Tomasi, J. *J. Chem. Phys.* **1997**, *107*, 3032–3041.
33. Tomasi, J.; Mennucci, B.; Cammi, R. *Chem. Rev.* **2005**, *105*, 2999–3094.
34. Caricato, M.; Mennucci, B.; Tomasi, J.; Ingrosso, F.; Cammi, R.; Corni, S.; Scalmani, G. *J. Chem. Phys.* **2006**, *124*, 124520–124513.
35. Frisch, M. J. et al. Gaussian 09 Revision D.01. Gaussian Inc. Wallingford CT 2009.
36. Mataga, N.; Kaifu, Y.; Koizumi, M. *Bull. Chem. Soc. Jpn.* **1956**, *29*, 465–470.
37. Haynes, W. M. *CRC handbook of chemistry and physics*; CRC press, 2014.
38. Würth, C.; Grabolle, M.; Pauli, J.; Spieles, M.; Resch-Genger, U. *Nat. Protoc.* **2013**, *8*, 1535–1550.
39. Strickler, S.; Berg, R. A. *J. Chem. Phys.* **1962**, *37*, 814–822.
40. Horng, M.-L.; Gardecki, J.; Maroncelli, M. *J. Phys. Chem. A* **1997**, *101*, 1030–1047.
41. Becker, W. *Advanced time-correlated single photon counting techniques*; Springer Science & Business Media, 2005; Vol. 81.
42. Rettig, W. *J. Phys. Chem.* **1982**, *86*, 1970–1976.
43. Englman, R.; Jortner, J. *Mol. Phys.* **1970**, *18*, 145–164.
44. Förster, T.; Hoffmann, G. *Z. Phys. Chem.* **1971**, *75*, 63–76.
45. Petrowsky, M.; Fleshman, A. M.; Frech, R. *J. Phys. Chem. B* **2013**, *117*, 2971–2978.
46. van Stokkum, I. H. M.; Larsen, D. S.; van Grondelle, R. *Biochim. Biophys.*

- Acta* **2004**, *1657*, 82–104.
47. Dreuw, A.; Head-Gordon, M. *Chem. Rev.* **2005**, *105*, 4009–4037.
48. Chai, J.-D.; Head-Gordon, M. *Phys. Chem. Chem. Phys.* **2008**, *10*, 6615–6620.
49. Massin, J.; Charaf-Eddin, A.; Appaix, F.; Bretonniere, Y.; Jacquemin, D.; Van Der Sanden, B.; Monnereau, C.; Andraud, C. *Chem. Sci.* **2013**, *4*, 2833–2843.